# Crystallization Behavior of $CaF_2$-$TiO_2$ Fluxes Geared Towards High Heat Input Submerged Arc Welding

Zhanjun Wang [a,b,c], Xiaorui Zheng [a,b], Ming Zhong [a,b], Zushu Li [d], Cong Wang [a,b]*

a. Key Laboratory for Ecological Metallurgy of Multimetallic Mineral (Ministry of Education), Northeastern University, Shenyang 110819, Liaoning, China

b. School of Metallurgy, Northeastern University, Shenyang 110819, China

c. State Key Laboratory of Advanced Metallurgy, University of Science and Technology Beijing, Beijing 100083, China

d. WMG, University of Warwick, Coventry, CV4 7AL, United Kingdom

* Corresponding author: wangc@smm.neu.edu.cn (Cong Wang)

Tel.: +86 15702435155 Fax: +86 24 23906316

**Abstract:**

Crystallization behaviors of $CaF_2$-$TiO_2$ fluxes with varying $TiO_2$ contents from 10 to 40 wt.% for high heat input submerged arc welding application have been systematically investigated by using single hot thermocouple technique (SHTT), field emission scanning electron microscopy (SEM), and X-ray diffraction (XRD). It is demonstrated that, as a function of the $TiO_2$ content, the crystallization temperature initially decreases (from 10 to 30 wt.%) but increases afterwards (>30 wt.%), while the incubation time follows an opposite trend. It has been confirmed that $CaTiO_3$ and $CaF_2$ are the two dominant precipitated phases. It is further shown that the growth of $CaTiO_3$

crystals follows a three-dimensional pattern while that of $CaF_2$ a two-dimensional one. The effective activation energy is the highest when the $TiO_2$ content is 30 wt.%, indicating the greatest barrier to crystallize and the highest capability to achieve the most desired production of amorphous welding fluxes for high heat input applications.

Keywords: High heat input; Submerged arc welding; Flux; Crystallization; $CaF_2$-$TiO_2$

## 1. Introduction

Possessing an array of prominent properties, including high specific strength, superior low-temperature impact toughness, suitable weldability, and excellent corrosion resistance, low carbon low alloy steel grades have been extensively employed in shipbuilding and offshore engineering settings [1-4]. With the imminent application of high heat input welding, an ever-evolving challenge is how to ensure the soundness of the weld joints, which may subject to premature failure inherent from the prolonged cooling and deteriorated microstructure [5-9].

In recent years, to further improve the overall mechanical performance of the weld metal under high heat input welding conditions, $TiO_2$-bearing welding fluxes have been designed and applied [10, 11]. It is generally believed that O content is a key parameter determining the microstructure and mechanical properties of weld joints, and welding flux is the main source of O supply in submerged arc welding [12]. The underlying philosophy is to, through fine-tuned transfer of Ti and O elements from the molten flux to the weld metal, promote the formation of Ti-containing inclusions, which may likely act as suitable intragranular nucleation sites for the formation of acicular ferrites,

thereby enhancing the mechanical responses *via* the interlocking nature [10]. Paniagua-Mercado et al. [13] found that increasing $TiO_2$ content in the welding flux could enhance the percentage of acicular ferrite that plays a significant role in heterogeneous nucleation and reduce the size of acicular ferrite. Roy et al. [14] observed that as the content of $TiO_2$ added to commercial welding fluxes increased from 2.5 wt.% to 12.5 wt.%, the average grain sizes of ferrite and pearlite decreased, while the percentage of ferrites in the weld metal increased at the expense of diminishing pearlites. Zhang et al. [10] and Kohno et al. [15] clarified that $TiO_2$ could promote the transfer of Ti and O elements to the weld metal, which could induce the formation of inclusions and increase the nucleation rate of acicular ferrite, thereby improving the strength and toughness of the weld metal.

According to Paniagua-Mercado et al. [16], Zhang et al. [11, 17] and Kim et al. [2, 7, 18], physicochemical properties of the welding flux, especially the crystallization features, could directly control alloying element transfer behaviors, affect the slag-metal reaction and the detachability (discrete separation of the flux from the metal after welding), and ultimately determine the quality of welding. Multiple studies suggested that the presence of $[Cr,Mn,Mg][Cr,Mn,Al]_2O_4$ spinel, or cordierite ($Mg_2Al_4Si_5O_{18}$) type structure, or $Cr_2TiO_5$ and $FeTiO_5$ phases were generally not conducive to slag detachability [19, 20]. Moreover, a higher crystallization temperature of the welding flux could narrow the temperature range of slag-metal reaction and influence alloying element transfer, and is not conducive to obtaining an amorphous flux with uniform composition that is beneficial for welding. $CaF_2$ has been widely employed for the

design of welding flux to improve the basicity and minimize the O potential [21, 22]. However, it needs to be pointed out that investigations focusing on the crystallization behavior of $TiO_2$-bearing welding fluxes have yet to be fully conducted to minimize unnecessary defects closely associated with alloying element transfer behaviors and slag-metal reactions in the weld zone. In this regard, considering the extensive application of $TiO_2$-bearing fluxes in the actual welding process, the present study is undertaken to explore the influence of $TiO_2$ content on the crystallization behaviors of the $CaF_2$-$TiO_2$ flux system. Furthermore, the kinetics and effective activation energy of the crystallization process will be fully investigated to facilitate the understanding and advance the design for $TiO_2$-bearing welding flux systems.

## 2. Experimental

### *2.1. Sample preparation*

Table 1 Pre- and post-experimental compositions of $CaF_2$-$TiO_2$ fluxes (wt.%).

| Sample | Pre-experimental composition | | Post-experimental composition | |
|---|---|---|---|---|
| | $TiO_2$ | $CaF_2$ | $TiO_2$ | $CaF_2$ |
| F10 | 10 | 90 | 10.66 (±0.12) | 89.34 (±0.14) |
| F20 | 20 | 80 | 20.95 (±0.19) | 79.05 (±0.35) |
| F30 | 30 | 70 | 31.66(±0.39) | 68.34 (±0.57) |
| F40 | 40 | 60 | 41.09 (±0.75) | 58.91 (±0.76) |

All experimental samples for $CaF_2$-$TiO_2$ fluxes were prepared using reagent grade powders of $CaF_2$ (>98.5 wt.%) and $TiO_2$ (>99 wt.%). The chemical compositions of the designed fluxes are provided in Table 1. Approximately 50 g samples were uniformly

mixed and premelted at 1550 °C in a molybdenum crucible with a matching lid under 0.3 L/min of Ar (> 99.999 %) flow. After 30 minutes, the premelted fluxes were rapidly quenched by cold water and crushed and ground into powders with the size less than 200 mesh. The chemical compositions of the premelted fluxes were confirmed by X-ray fluorescence (XRF, ZXS Priums II, Rigaku, Japan) and ethylene diamine tetraacetic acid (EDTA) titration method, as shown in Table 1, where the measured values showed negligible differences comparing with the weighed ones.

### *2.2. SHTT, XRD and SEM analysis*

Single hot thermocouple technique (SHTT) was employed to investigate the crystallization behavior of $CaF_2$-$TiO_2$ welding fluxes, and detailed descriptions of the technique can be found elsewhere [23, 24]. Approximately 0.01 g of the flux was placed on the tip of a B-type thermocouple (0.5 mm in diameter, Pt-30%Rh) with a controlled temperature program. The temperature of the thermocouple was calibrated in advance with pure $K_2SO_4$ with a constant melting point, where the calibration procedure was repeated 3 times to ensure ±1 °C temperature accuracy. The relationship between the temperature, time and precipitated crystals was simultaneously recorded by a microscope equipped with a video camera, where the SHTT images of primary phase can be used to construct continuous-cooling-transformation (CCT) and time-temperature-transformation (TTT) curves. It should be noted that the crystallization temperature and incubation time detected from the observed SHTT images were the average values from 3 parallel trials.

After SHTT experiment, fluxes solidified on the tip of the thermocouple were carefully mounted, polished, and carbon-coated for scanning electron microscopy (SEM, MIRA3, TESCAN, Czech) analysis to determine the morphology and composition of the crystalline fluxes. Crystalline phases of the fluxes were confirmed by X-ray diffraction (XRD, D8 Advance, Bruker, Germany) analysis using Cu Kα radiation at a voltage of 40 kV and a current of 30 mA with the 2-theta scanning range between 10° and 80° at a scanning rate of 2°/min and an increment of 0.02°. It should be noted that the amount of the flux after each single SHTT experiment was not adequate for XRD characterization. Therefore, 10 experiments under identical conditions were repeated to collect sufficient amount of flux samples for XRD (minimum requirement 0.1 g).

### *2.3. Analysis of kinetics and effective activation energy of the crystallization process*

The non-isothermal crystallization kinetics involving nucleation and growth kinetics can be described by the modified Johnson-Mehl-Avrami (JMA) model [25], as shown in equation (1):

$$\ln(-\ln(1-X)) = n\ln t + \beta \ln Z_c \quad (1)$$

where $X$ is the relative degree of crystallinity, $\beta$ (°C/s) is the cooling rate, $Z_c$ ($s^{-n}$/°C) is the modified crystallization rate constant, $t$ (s) is the crystallization time, and $n$ is Avrami constant, respectively. The calculated method of relative degree of crystallinity ($X$) can be found elsewhere [24]. The value of n can be obtained from the slope of the straight line by plotting ln(-ln(1-$X$)) vs. ln$t$.

The differential iso-conversional method proposed by Friedman [26] was used to calculate the dependence of effective activation energy on crystallinity, which is expressed as follows,

$$\ln\left(\frac{dX}{dt}\right)_X = -\frac{E_X}{RT_X} + C \quad (2)$$

where $(dX/dt)_X$ is the instantaneous crystallization rate at a given relative crystallinity, $T_x$ (K) is the temperature related to the given relative crystallinity at different cooling rates, $R$ (J·mol$^{-1}$·K$^{-1}$) is the gas constant, and $E_x$ (kJ/mol) is the effective activation energy for crystallization at a given relative degree of crystallinity, respectively. The effective activation energy can be determined from the slope of the fitted line between natural logarithm of instantaneous crystallization rate $\ln(dX/dt)_X$ vs. reciprocal temperature ($1/T_x$).

## 3. Results and discussion

### *3.1. CCT and TTT diagrams*

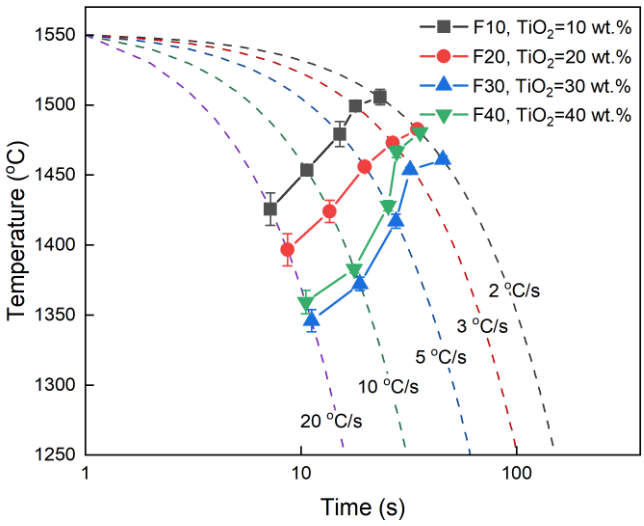


Fig. 1 CCT diagram of $CaF_2$-$TiO_2$ fluxes with different $TiO_2$ contents.

Using the initial crystallization images from the SHTT experiments, the CCT and TTT diagrams could be constructed for $CaF_2$-$TiO_2$ fluxes. The CCT diagrams of $CaF_2$-$TiO_2$ fluxes with different $TiO_2$ contents are shown in Fig. 1 for cooling rates of 2 °C/s, 3 °C/s, 5 °C/s, 10 °C/s and 20 °C/s starting from 1550 °C. It can be observed that the crystallization temperature initially decreases with increasing $TiO_2$ content from 10 wt.% to 30 wt.%, and then increases with further addition of $TiO_2$ content up to 40 wt.%, which may be caused by the generation of significant amount of crystalline phases with high melting points.[27] In addition, as the cooling rate increases, the initial crystallization temperature of $CaF_2$-$TiO_2$ fluxes shift towards lower temperature, which can be attributed to the competing factors of: a) accelerated nucleation and growth of crystals under higher degree of undercooling, and b) inhibited growth of the crystals due to increased viscosity and concurrently lowered diffusivity [28, 29].

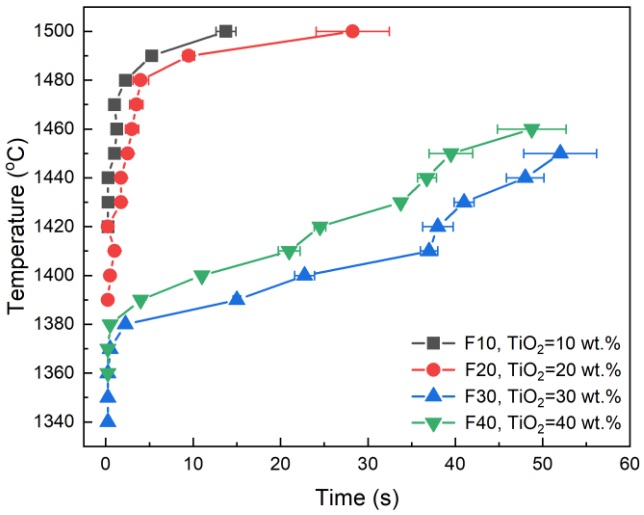


Fig. 2 TTT diagram of $CaF_2$-$TiO_2$ fluxes with different $TiO_2$ contents.

Fig. 2 shows the TTT diagrams of $CaF_2$-$TiO_2$ fluxes with different $TiO_2$ contents. The TTT curves of all fluxes exhibit a half "C"-shape, indicating that a single crystal

phase has been formed during the isothermal crystallization process. The incubation time obtained from TTT curves is an important parameter to characterize the crystallization properties of different fluxes, where a longer incubation time generally indicates an inhibited crystallization process [30]. It can be seen that under the same isothermal crystallization condition, with the increase of $TiO_2$ content from 10 to 30 wt.%, the crystallization incubation time is prolonged; with further addition of $TiO_2$ content to 40 wt.%, the incubation time becomes shorter, implying the inhibition and acceleration of the crystallization process, respectively. For the same flux, as the isothermal temperature decreases, the undercooling of the flux increases, resulting in a greater driving force for nucleation, which is manifested in the reduced incubation time and accelerated crystallization [28, 31]. Thus, it can be concluded that when the $TiO_2$ content is 30 wt.%, the crystallization capacity of $CaF_2$-$TiO_2$ fluxes is inhibited the most, which correlates well with the crystallization temperature shown in CCT curves and the incubation time shown in TTT diagrams. In addition, it is noteworthy that as the isothermal temperature decreases, the crystallization incubation time gradually decreases to close to 0 seconds, indicating that the critical cooling rate of respective $CaF_2$-$TiO_2$ flux is extremely high, which is not beneficial to obtain amorphous welding flux, and may require further adjustment [29, 32].

### *3.2. Determination of crystalline phases*

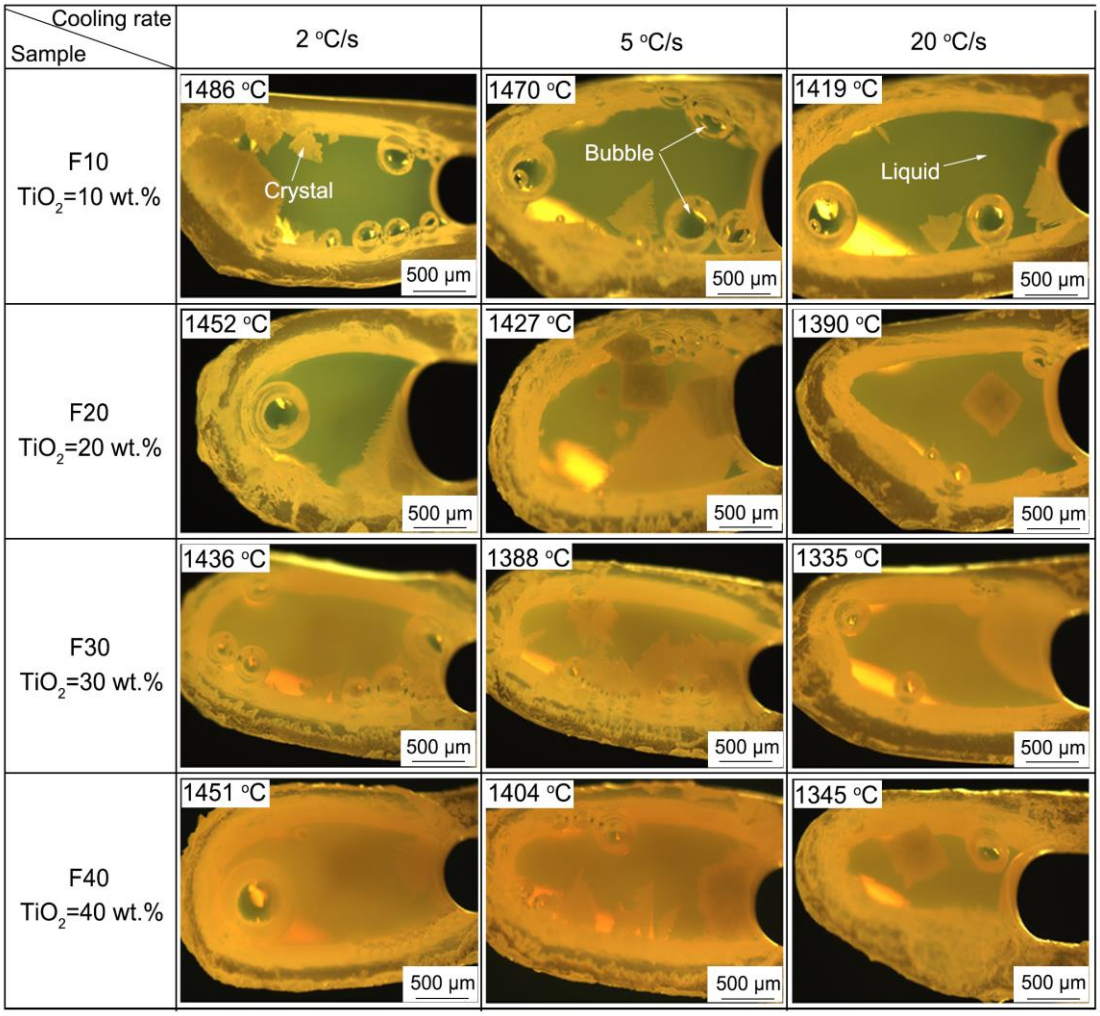


Fig. 3 Typical SHTT images of $CaF_2$-$TiO_2$ fluxes with different $TiO_2$ contents at different cooling rates.

Fig. 3 shows typical SHTT images for $CaF_2$-$TiO_2$ fluxes continuously cooled at the constant rates of 2 °C/s, 5 °C/s, and 20 °C/s, respectively. It can be seen that when the cooling rate is fixed at 2 °C/s, dendritic crystals initially grow along the edge of the thermocouple and continue to grow towards the center of the liquid phase. According to the theory of heterogeneous nucleation, when a new phase nucleates on the surface of the existing solid particles, the energy required for nucleation is significantly reduced

[33, 34]. With the increase of cooling rate, nucleation features change, where dendritic and cloud-like crystals begin to appear in the center of certain fluxes with high $TiO_2$ contents. However, it appears that, for fluxes with high $TiO_2$ contents, the relatively high crystallization rate renders it difficult to capture subtle crystalline characteristics. In addition, in the actual welding process, it is essential to avoid the excessively rapid crystallization process, which may delay or even inhibit the transfer of alloying elements incurred by slag-metal reactions [21, 22, 35].

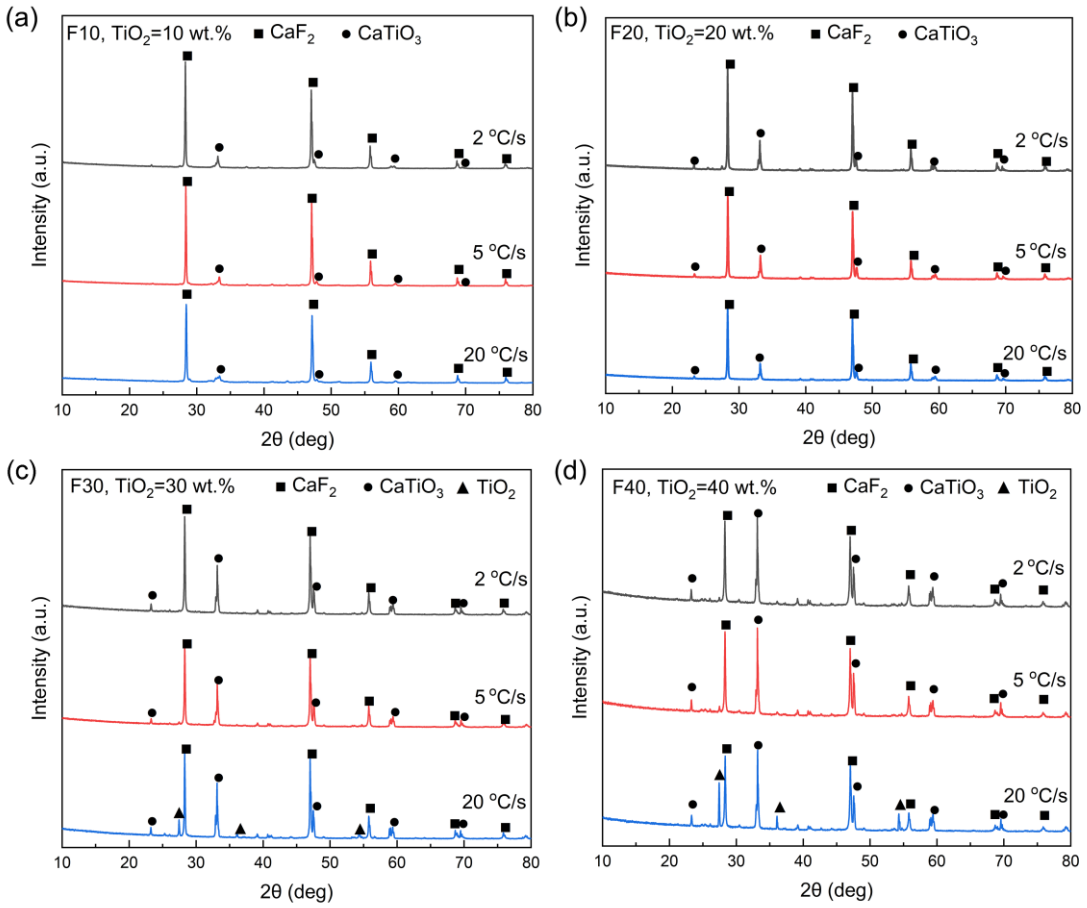


Fig. 4 XRD patterns of $CaF_2$-$TiO_2$ fluxes with different $TiO_2$ contents at cooling rates of 2 °C/s, 5 °C/s and 20 °C/s. (a) F10, $TiO_2$=10 wt.%, (b) F20, $TiO_2$=20 wt.%, (c) F30, $TiO_2$=30 wt.%, (d) F40, $TiO_2$=40 wt.%.

Fig. 4 displays the XRD patterns of $CaF_2$-$TiO_2$ fluxes under different cooling rates.

It can be seen that $CaF_2$ and $CaTiO_3$ can be detected for fluxes with $TiO_2$ contents of 10 wt.% and 20 wt.% under cooling rates of 2 °C/s, 5 °C/s and 20 °C/s. When the $TiO_2$ content is increased further to 30 wt.% and 40 wt.%, $TiO_2$ peaks appear and are more obvious at higher cooling rates.

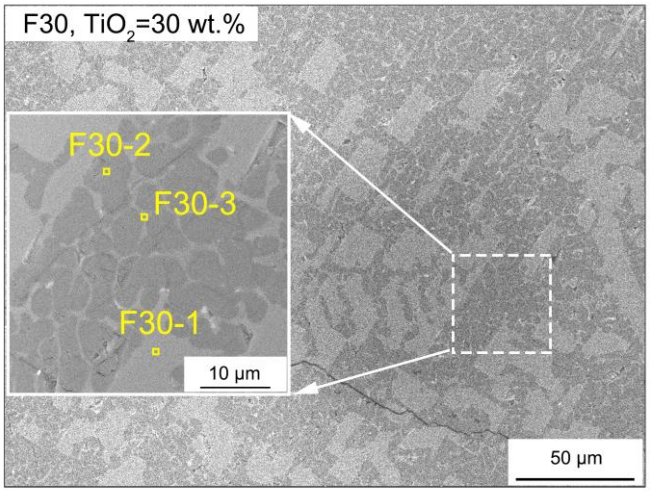


at.%

| Point | Ca | F | Ti | O | Phase |
|---|---|---|---|---|---|
| F30-1 | 21.8(±0.67) | 0 | 22.8(±0.95) | 55.4(±2.07) | $CaTiO_3$ |
| F30-2 | 33.2(±1.27) | 66.8(±1.29) | 0 | 0 | $CaF_2$ |
| F30-3 | 22.8(±1.42) | 39.6(±1.74) | 11.4(±1.22) | 26.2(±1.60) | Matrix |

Fig. 5 Typical SEM image of sample F30 after SHTT measurement at the cooling rate of 2 °C/s and corresponding EDS results. Inset figure is the enlarged region of the interested area denoted by the dashed square.

Fig. 5 shows the typical SEM image and corresponding EDS point analysis results of the $CaF_2$-$TiO_2$ flux continuously cooled at 2 °C/s. It can be seen that, from a semi-quantitative perspective, salient regions can be categorized as $CaTiO_3$ (F30-1), $CaF_2$ (F30-2) and the amorphous matrix (F30-3), respectively, coinciding well with XRD results.

Based on the results above, it can be concluded that the addition of $TiO_2$ can

promote the formation of $CaTiO_3$. According to Hao et al. [36], the presence of $CaTiO_3$ could effectively increase the heat flux of the welding flux, thereby promoting the heat to diffuse outside the welding flux shell and to prevent the heat from accumulating in the weld metal, which may likely lead to the formation of coarse grains deteriorating low-temperature impact toughness of the weld metal. In addition, the formation of $CaTiO_3$ with a strong directional dendritic morphology can facilitate the separation of the slag shell from the weld metal [37].

### *3.3. Nucleation and growth of different crystalline phases*

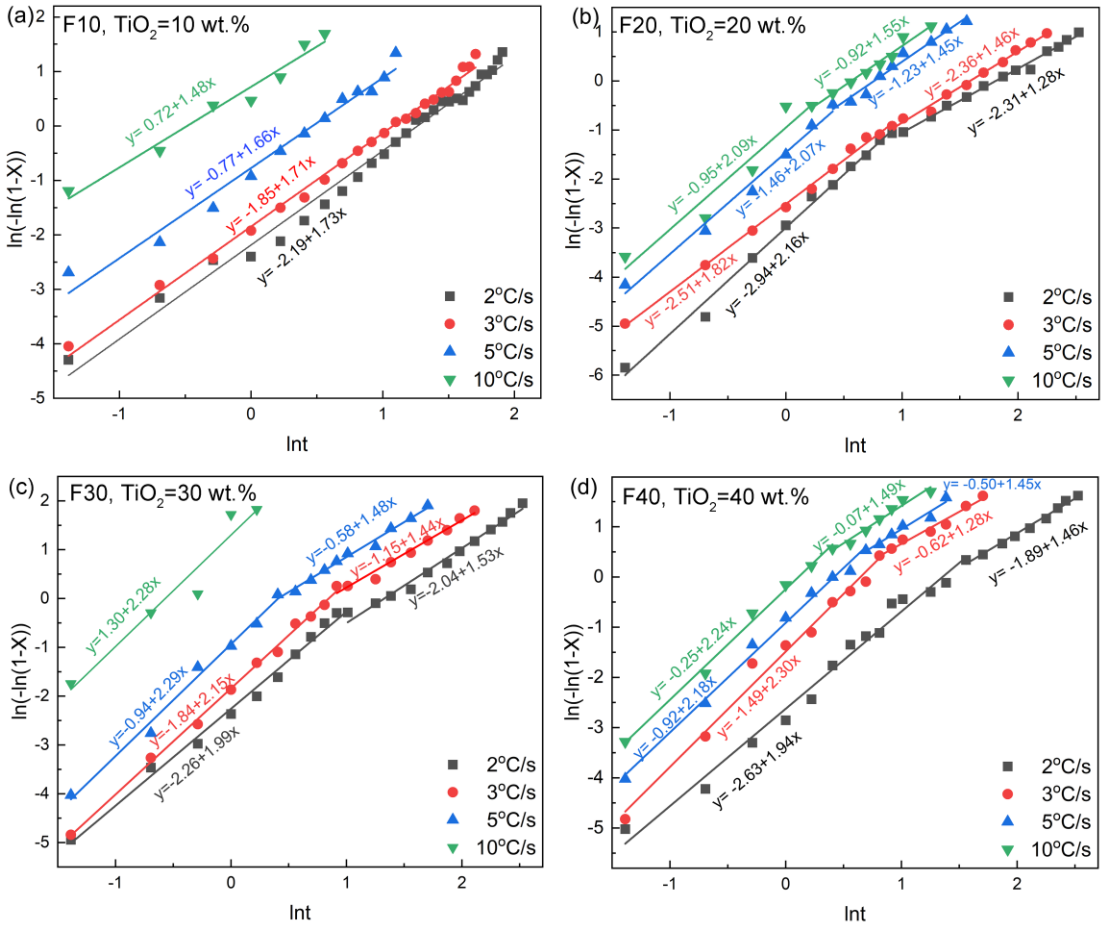


Fig. 6 Plots of ln(-ln(1-*X*)) vs. ln*t* for non-isothermal crystallization of $CaF_2$-$TiO_2$ fluxes at different cooling rates. (a) F10, $TiO_2$=10 wt.%, (b) F20, $TiO_2$=20 wt.%, (c) F30, $TiO_2$=30 wt.%, (d) F40, $TiO_2$=40 wt.%.

The relative crystallinity as a function of temperature at different cooling rates is presented in Supplemental Materials Fig. S1. Based on this, Fig. 6 is established to display the relationship between ln(-ln(1-X)) and lnt at different cooling rates, aiming to analyze the kinetics of the non-isothermal crystallization process. It can be observed that, for the 10 wt.% $TiO_2$ flux (Fig. 6(a)), all fitted lines are approximately straight without noticeable inflection points. However, nearly all fitted lines of other fluxes can be divided into two distinctive portions separated by outstanding inflection points, which indicate the precipitation of different crystalline phases. According to Zhou et al. [38] and Zheng et al. [39], these phases can be identified as $CaTiO_3$ and $CaF_2$, respectively. It should be noted that the flux composition with 30 wt.% $TiO_2$ is located at the eutectic point of $CaF_2$-$TiO_2$ phase diagram [40, 41]. When the cooling rate is 10 °C/s, the crystallization process of the flux with 30 wt.% $TiO_2$ is extremely fast and can be completed within 1.5 seconds, which is difficult to obtain the two different crystallization stages from the fitted line of ln(-ln(1-$X$)) vs. ln$t$ due to limited data. Thus, the fitted lines of welding flux with 10 wt.% $TiO_2$ at all cooling rates and the fitted line of welding flux with 30 wt.% $TiO_2$ at the cooling rate of 10 °C/s is not used for such analysis.

Table 2 The values of Avrami constant ($n$) of $CaF_2$-$TiO_2$ fluxes at different cooling rates.

| Sample No. | Cooling Rate (°C/s) | Avrami Constant ($n$) | |
|---|---|---|---|
| | | Primary Crystallization Stage | Secondary Crystallization Stage |
| F20 | 2 | 2.157 | 1.281 |
| | 3 | 1.815 | 1.455 |
| | 5 | 2.074 | 1.454 |
| | 10 | 2.092 | 1.545 |
| | Average | 2.035 | 1.434 |
| F30 | 2 | 1.993 | 1.534 |
| | 3 | 2.151 | 1.443 |
| | 5 | 2.292 | 1.479 |
| | 10 | - | - |
| | Average | 2.145 | 1.485 |
| F40 | 2 | 1.936 | 1.464 |
| | 3 | 2.297 | 1.284 |
| | 5 | 2.183 | 1.448 |
| | 10 | 2.242 | 1.486 |
| | Average | 2.165 | 1.421 |

The values of the Avrami constant ($n$) can be estimated from the slope of the fitted lines, as summarized in Table 2. It is generally accepted that the nucleation and growth mechanism of crystallization is related to the Avrami constant, as shown in Equation (3) [42],

$$n = a + bc \quad (3)$$

where "$a$" is a constant associated with the nucleation rate ($0 < a < 1$ means a decreasing nucleation rate with holding time, $a = 1$ means a constant nucleation rate, and $a > 1$ means an increasing nucleation rate with holding time), "$b$" is a constant related to the growth dimension of the crystals ($b = 1$ means one-dimensional growth, $b = 2$ means two-dimensional growth, and $b = 3$ means three-dimensional growth), and "$c$" is a

253 constant related to the growth rate of the crystals ($c$ = 1 means interface-controlled
254 growth and $c$ = 0.5 means diffusion-controlled growth). According to Li et al. [42], the
255 growth of $CaTiO_3$ shows typical three-dimensional growth pattern, *i.e.*, $b$ can be
256 considered as 3. According to Lou et al. [43], the growth of $CaTiO_3$ is diffusion-
257 controlled, *i.e.*, $c$ equals to 0.5. Thus, combining the value of Avrami constant in the
258 crystallization primary stage shown in Table 2, it can be estimated that $a$ is less than 1,
259 suggesting the nucleation rate of $CaTiO_3$ decreases with holding time. In addition,
260 according to Shi et al. [44], the growth of $CaF_2$ follows a two-dimensional growth
261 pathway, *i.e.*, $b$ equals to 2. Combining all the Avrami constants of $CaF_2$ crystals less
262 than 2, it can be interpreted that $c$ is 0.5 and $a$ is less than 1, indicating that the
263 crystallization of $CaF_2$ occurs through diffusion-controlled mechanism and the
264 nucleation rate of $CaF_2$ decreases with holding time. The presence of $CaTiO_3$ is
265 beneficial for welding flux detachability [37]. However, considering the significance of
266 the amorphous state for the uniformity of the flux composition and rapid crystallization
267 of $CaTiO_3$ goes against obtaining the amorphous welding flux, the viscosity of the
268 welding fluxes and the nucleation rate of $CaTiO_3$ should be further optimized in the
269 future.

### *3.4. Effective activation energies for non-isothermal crystallization*

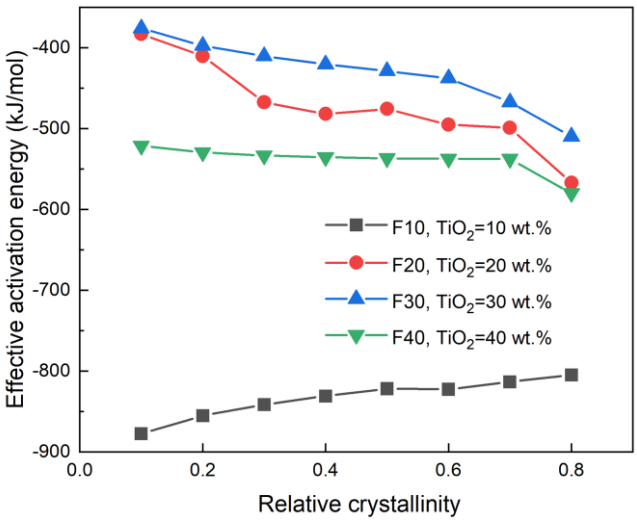


Fig. 7 The effective activation energy in non-isothermal crystallization at different relative crystallinity.

Fig. 7 shows the effective activation energy in non-isothermal crystallization of $CaF_2$-$TiO_2$ fluxes as a function of the whole relative crystallinity. The effective activation energy of flux with 30 wt.% $TiO_2$ during the entire crystallization process is higher than that of other fluxes. It has been reported that higher activation energy means a greater barrier to orderly structure formation [45]. Thus, it can be deduced that the flux with 30 wt.% $TiO_2$ has the lowest crystallization tendency, which is consistent with the lowest crystallization temperature and the longest incubation time in the CCT and TTT diagrams. In addition, it can be observed that as the relative crystallinity increases, the effective activation energy of flux with 10 wt.% $TiO_2$ gradually increases, whereas the effective activation energies of fluxes with $TiO_2$ contents of 20 wt.%, 30 wt.% and 40 wt.% gradually decrease. The temperature decreases as the relative crystallinity

increases. According to the classical nucleation theory [46], the thermodynamic barrier decreases and the undercooling increases with decreasing temperature. Thus, as the relative crystallinity increases, the effective activation energies of fluxes with $TiO_2$ contents of 20 wt.%, 30 wt.% and 40 wt.% gradually decrease. However, for the flux containing 10 wt.% $TiO_2$, it is likely that as the temperature decreases, the driving force for diffusion is depreciated, which, in turn, leads to an increase in the effective activation energy.

Furthermore, it should be mentioned that for $CaF_2$-$TiO_2$ flux with $TiO_2$ content of 30 wt.%, the Ti content in the weld metal reaches the maximum value during the actual welding process, which can induce the formation of Ti-bearing inclusions to facilitate the formation of acicular ferrite in appreciable quantities, thereby improving mechanical properties of the weld metal.[22, 47] Thus, $CaF_2$-$TiO_2$-based fluxes with the $CaF_2/TiO_2$ mass ratio of 7:3 should be encouraged for designing and optimizing the welding flux.

## 4. Conclusions

This study focuses on the influence of $TiO_2$ content on the crystallization behavior of $CaF_2$-$TiO_2$ fluxes. The main conclusions can be summarized as follows:

(1) With increasing $TiO_2$ content, the crystallization temperature initially decreases with increasing $TiO_2$ content from 10 to 30 wt.% and subsequently increases with further addition of $TiO_2$ content up to 40 wt.%, whereas the incubation time follows an opposite trend.

(2) The addition of $TiO_2$ can promote the formation of $CaTiO_3$ with dendritic morphology. The nucleation rate of $CaTiO_3$ decreases with holding time and the growth of $CaTiO_3$ crystals follows a three-dimensional diffusion-controlled pattern.

(3) The effective activation energy of the flux containing 30 wt.% $TiO_2$ during the entire crystallization process is higher than that of other fluxes, indicating that the flux with 30 wt.% $TiO_2$ has the lowest crystallization capacity.


## Acknowledgment

The authors sincerely thank the National Natural Science Foundation of China (Grant Nos. 52104295, U20A20277, 52050410341, 52011530180, 52150610494), Royal Academy of Engineering (Grant No. TSPC1070), Royal Society (Grant No. IEC/NSFC/191318), Research Fund for Central Universities (Grant Nos. N2025025, N2125016). This work is also funded by the Regional Innovation Joint Fund of Liaoning Province (Grant No. 2020-YKLH-39) and the Open Foundation of State Key Laboratory of Advanced Metallurgy, University of Science and Technology Beijing (Grant No. KF21-02).


## Credit authorship contribution statement

**Zhanjun Wang**: Data curation, Formal analysis, Methodology, Writing - review & editing; **Xiaorui Zheng**: Data curation, Writing - original draft; **Ming Zhong**: Writing - review; **Zushu Li**: Writing - review; **Cong Wang**: Supervision, Resources, Writing - review & editing, Funding acquisition.

## Declaration of Competing Interest

The authors declare that they have no known competing financial interests or personal relationships that could have appeared to influence the work reported in this paper.

## Supplemental material

The online version of this article contains Supplemental Materials, which is available to authorized users.

## References


[1] J. Zhang, T. Coetsee, H. Dong, C. Wang, Elucidating the roles of $SiO_2$ and MnO upon decarburization during submerged arc welding: A thermodynamic study into EH36 shipbuilding steel, Metall. Mater. Trans. B, 51 (2020) 1805-1812.

[2] J. Kim, I. Sohn, Influence of $TiO_2$/$SiO_2$ and MnO on the viscosity and structure in the $TiO_2$-MnO-$SiO_2$ welding flux system, J. Non-Cryst. Solids, 379 (2013) 235-243.

[3] Z. Wang, J. Zhang, M. Zhong, C. Wang, Insight into the viscosity-structure relationship of MnO-$SiO_2$-MgO-$Al_2O_3$ fused submerged arc welding flux, Metall. Mater. Trans. B, 53 (2022) 1364-1370

[4] X. Zou, L. Zhou, H. Matsuura, C. Wang, Understanding the role of Ti in particle

347 formation and microstructure refinement in Fe-CO-Ti alloys, JOM, 73 (2021)
348 1110-1117.
349 [5] L. Wang, G. Zhang, J. Xu, Y. Li, Q. Chen, Y. Rong, Y. Huang, Effect of welding
350 parameters on the geometry, microstructure, and corrosion resistance of laser
351 welded 16 mm EH40 joints, Metall. Mater. Trans. B, 52 (2021) 3930-3937.
352 [6] J. Zhang, C. Wang, T. Coetsee, Thermodynamic evaluation of element transfer
353 behaviors for fused CaO-$SiO_2$-MnO fluxes subjected to high heat input
354 submerged arc welding, Metall. Mater. Trans. B, 52 (2021) 1937-1944.
355 [7] J. Kim, J. Choi, I. Han, I. Sohn, High-temperature wettability and structure of
356 the $TiO_2$-MnO-$SiO_2$-$Al_2O_3$ welding flux system, J. Non-Cryst. Solids, 432
357 (2016) 218-226.
358 [8] C. Wang, J. Zhang, Fine-tuning weld metal compositions via flux optimization
359 in submerged arc welding: an overview, Acta Metall. Sin., 57 (2021) 1126-1140.
360 [9] X. Xu, Z. Ming, Z. Tan, W. Cong, Probing microstructural evolution in weld
361 metals subject to varied $CaF_2$-$TiO_2$ flux cored wires under high heat input
362 electro-gas welding, J. Iron. Steel Res. Int., (2022) Accepted.
363 [10] J. Zhang, T. Coetsee, S. Basu, C. Wang, Impact of gas formation on the transfer
364 of Ti and O from $TiO_2$-bearing basic-fluoride fluxes to submerged arc welded
365 metals: A thermodynamic approach, Calphad, 71 (2020) 102195.
366 [11] J. Zhang, J. Leng, C. Wang, Tuning weld metal mechanical responses via
367 welding flux optimization of $TiO_2$ content: Application into EH36 shipbuilding
368 steel, Metall. Mater. Trans. B, 50 (2019) 2083-2087.

[12] T. Eagar, Sources of weld metal oxygen contamination during submerged arc welding, Weld. J., 57 (1978) 76-80.

[13] A.M. Paniagua-Mercado, V.M. Lopez-Hirata, H.J. Dorantes-Rosales, P.E. Diaz, E.D. Valdez, Effect of $TiO_2$-containing fluxes on the mechanical properties and microstructure in submerged-arc weld steels, Mater. Charact., 60 (2009) 36-39.

[14] J. Roy, R.N. Rai, S.C. Saha, Effect of $TiO_2$ enriched fluxes on the bead geometry, grain size and hardness in submerged arc welds, Int. J. Mater. Prod. Tech., 56 (2018) 313-325.

[15] R. Kohno, T. Takami, N. Mori, K. Nagano, New fluxes of improved weld metal toughness for HSLA steels, Weld. J., 61 (1982) 373-380.

[16] A.M. Paniagua-Mercado, P. Estrada-Diaz, V.M. Lopez-Hirata, Chemical and structural characterization of the crystalline phases in agglomerated fluxes for submerged-arc welding, J. Mater. Process. Tech., 141 (2003) 93-100.

[17] J. Zhang, T. Coetsee, H. Dong, C. Wang, Fine-tuned element transfer strategies for ternary $CaF_2$-$SiO_2$-CaO fluxes in submerged arc welding: an environmentally friendly approach, Metall. Mater. Trans. B, 51 (2020) 1350-1354.

[18] J.B. Kim, I. Sohn, Effect of alumina and extended basicity on the viscosity and structure in the $TiO_2$-MnO-$Al_2O_3$-8.64 $ZrO_2$-2.77 $Na_2O$ welding flux system, ISIJ Int., 54 (2014) 657-663.

[19] H. Wang, R. Qin, G. He, $SiO_2$ and $CaF_2$ behavior during shielded metal arc welding and their effect on slag detachability of the CaO-$CaF_2$-$SiO_2$ type

391 ENiCrFe-7-covered electrode, Metall. Mater. Trans. A, 47 (2016) 4530-4542.
392 [20] D. Olson, G. Edwards, S. Marya, Physical and chemical phenomena influencing
393 slag detachability during welding, Key Eng. Mater., 69 (1992) 253-268.
394 [21] C.S. Chai, T.W. Eagar, Slag metal reactions in binary $CaF_2$-metal oxide welding
395 fluxes, Weld. J., 61 (1982) 229-232.
396 [22] J. Zhang, T. Coetsee, H. Dong, C. Wang, Element transfer behaviors of fused
397 $CaF_2$-$TiO_2$ fluxes in EH36 shipbuilding steel during high heat input submerged
398 arc welding, Metall. Mater. Trans. B, 51 (2020) 1953-1957.
399 [23] C. Yang, G. Wen, X. Zhu, P. Tang, In situ observation and numerical simulation
400 of bubble behavior in CaO-$SiO_2$ based slag during isothermal and
401 nonisothermal processes, J. Non-Cryst. Solids, 464 (2017) 56-72.
402 [24] L. Zhou, H. Li, W. Wang, J. Chang, Nonisothermal crystallization kinetics of
403 glassy mold fluxes, Metall. Mater. Trans. B, 49 (2018) 3019-3029.
404 [25] A. Jeziorny, Parameters characterizing the kinetics of the non-isothermal
405 crystallization of poly(ethylene terephthalate) determined by d.s.c, Polymer, 19
406 (1978) 1142-1144.
407 [26] Q. Shu, J.L. Klug, Q. Li, Non-isothermal melt crystallization kinetics for CaO-
408 $Al_2O_3$-$B_2O_3$ F-free mould fluxes, ISIJ Int., 59 (2019) 1057-1063.
409 [27] K. Zheng, Z. Zhang, L. Liu, X. Wang, Investigation of the viscosity and
410 structural properties of CaO-$SiO_2$-$TiO_2$ slags, Metall. Mater. Trans. B, 45 (2014)
411 1389-1397.
412 [28] J. Yang, J. Zhang, O. Ostrovski, C. Zhang, D. Cai, Effects of $B_2O_3$ on

crystallization, structure, and heat transfer of $CaO-Al_2O_3$-based mold fluxes, Metall. Mater. Trans. B, 50 (2019) 291-303.

[29] Z. Wang, I. Sohn, Effect of the $Al_2O_3/SiO_2$ mass ratio on the crystallization behavior of $CaO-SiO_2-MgO-Al_2O_3$ slags using confocal laser scanning microscopy, Ceram. Int., 44 (2018) 19268-19277.

[30] B. Lu, K. Chen, W. Wang, B. Jiang, Effects of $Li_2O$ and $Na_2O$ on the crystallization behavior of lime-alumina-based mold flux for casting high-Al steels, Metall. Mater. Trans. B, 45 (2014) 1496-1509.

[31] S.S. Jung, I. Sohn, Crystallization behavior of the $CaO-Al_2O_3-MgO$ system studied with a confocal laser scanning microscope, Metall. Mater. Trans. B, 43 (2012) 1530-1539.

[32] H. Tian, Z. Wang, T. Zhao, C. Wang, A Raman and multinuclear $^{29}Si$, $^{27}Al$, and $^{19}F$ NMR study on the structural roles of $CaF_2$ in $SiO_2-CaO-Al_2O_3$-based welding fluxes, Metall. Mater. Trans. B, 53 (2022) 232-241.

[33] Y. Sun, Z. Li, L. Liu, X. Wang, Z. Zhang, Co-modification and crystalline-control of Ti-bearing blast furnace slags, ISIJ Int., 55 (2015) 158-165.

[34] J. Yang, J. Zhang, Y. Sasaki, O. Ostrovski, C. Zhang, D. Cai, Y. Kashiwaya, In-situ study of crystallisation behaviour of $CaO-SiO_2-Na_2O-B_2O_3-TiO_2-Al_2O_3-MgO-Li_2O$ fluorine-free mould fluxes with different $CaO/SiO_2$ ratios, ISIJ Int., 56 (2016) 574-583.

[35] J. Jang, J. Indacochea, Inclusion effects on submerged-arc weld microstructure, J. Mater. Sci., 22 (1987) 689-700.

435 [36] Z. Hao, W. Chen, C. Lippold, Effect of titania absorption into a mold flux on
436 the heat transfer between the mold and the slab in the continuous casting of
437 titanium-stabilized stainless steel, Metall. Mater. Trans. B, 41 (2010) 805-812.
438 [37] P. Li, G. Meng, Effect of $TiO_2$ on detachability of stainless steel electrode, Trans.
439 China Weld. Inst., 27 (2006) 69-72.
440 [38] L. Zhou, H. Li, W. Wang, J. Chang, Nonisothermal crystallization kinetics of
441 glassy mold fluxes, Metall Mater Trans B, 49 (2018) 3019-3029.
442 [39] D. Zheng, J. Li, C. Shi, J. Ju, Crystallization characteristics and in-mold
443 performance of electroslag remelting-type $TiO_2$-bearing slag, Metall Mater
444 Trans B, 50 (2019) 1148-1160.
445 [40] V.D. Eisenhüttenleute, Slag Atlas, 2nd Edition ed., Verlag Stahleisen GmbH,
446 Düsseldorf, Germany, 1995.
447 [41] L. Hillert, H. Bo, A. Magnéli, A. Kallner, The phase diagram (81% $TiO_2$+19%
448 CaO)-$CaF_2$, Acta Chemica. Scand., 19 (1965) 1986-1987.
449 [42] J. Li, Z. Zhang, L. Liu, W. Wang, X. Wang, Influence of basicity and $TiO_2$
450 content on the precipitation behavior of the Ti-bearing blast furnace slags, ISIJ
451 Int., 53 (2013) 1696-1703.
452 [43] T. Lou, Y. Li, L. Li, Z. Sui, Study on kinetics of perovskite phase precipitate in
453 slag bearing titanium, J. China Ceram. Soc., 28 (2000) 255-258.
454 [44] C. Shi, M. Seo, H. Wang, J. Cho, S. Kim, Crystallization kinetics and
455 mechanism of CaO-$Al_2O_3$-based mold flux for casting high-aluminum TRIP
456 steels, Metall. Mater. Trans. B, 46 (2015) 345-356.

[45] M. Dapiaggi, G. Artioli, C. Righi, R. Carli, High temperature reactions in mold flux slags: Kinetic versus composition control, J. Non-Cryst. Solids, 353 (2007) 2852-2860.

[46] V.M. Fokin, E.D. Zanotto, N.S. Yuritsyn, J.W. Schmelzer, Homogeneous crystal nucleation in silicate glasses: A 40 years perspective, J. Non-Cryst. Solids, 352 (2006) 2681-2714.

[47] X. Yuan, M. Zhong, Y. Wu, C. Wang, Characterizing inclusions in the weld metal of EH36 shipbuilding steel processed by $CaF_2$-30 wt pct $TiO_2$ Flux, Metall. Mater. Trans. B, 53 (2022) 656-661.

**Table and Figure captions:**

Table 1 Pre- and post-experimental compositions of $CaF_2$-$TiO_2$ fluxes (wt.%).

Table 2 The values of Avrami constant ($n$) of $CaF_2$-$TiO_2$ fluxes at different cooling rates.

Fig. 1 CCT diagram of $CaF_2$-$TiO_2$ fluxes with different $TiO_2$ contents.

Fig. 2 TTT diagram of $CaF_2$-$TiO_2$ fluxes with different $TiO_2$ contents.

Fig. 3 Typical SHTT images of $CaF_2$-$TiO_2$ fluxes with different $TiO_2$ contents at different cooling rates.

Fig. 4 XRD patterns of $CaF_2$-$TiO_2$ fluxes with different $TiO_2$ contents at cooling rates of 2 °C/s, 5 °C/s and 20 °C/s. (a) F10, $TiO_2$=10 wt.%, (b) F20, $TiO_2$=20 wt.%, (c) F30, $TiO_2$=30 wt.%, (d) F40, $TiO_2$=40 wt.%.

Fig. 5 Typical SEM image of sample F30 after SHTT measurement at the cooling rate of 2 °C/s and corresponding EDS results. Inset figure is the enlarged region of the interested area denoted by the dashed square.

Fig. 6 Plots of $\ln(-\ln(1-X))$ vs. $\ln t$ for non-isothermal crystallization of $CaF_2$-$TiO_2$ fluxes

488 at different cooling rates. (a) F10, $TiO_2$=10 wt.%, (b) F20, $TiO_2$=20 wt.%, (c) F30,

489 $TiO_2$=30 wt.%, (d) F40, $TiO_2$=40 wt. %.

490

491 Fig. 7 The effective activation energy in non-isothermal crystallization at different

492 relative crystallinity.